Supplementary Information (SI) for Nanoscale.

Out-of-Plane Strain Induced Non-Thermal Bandgap Tuning of Black Phosphorus On-Chip Devices

Xiaotong Yu[1], Yuxin Gao[1], Zizhou Xia[2], Xinwei Li[1], Zhiyuan Wang[1], Yuan Gao[1]*, Jean-Jacques Delaunay[2]*, Zhiyu Wang[1]*

[1]School of Mechanical Science and Engineering, Huazhong University of Science and Technology, Wuhan, China. E-mail: yuan_gao@hust.edu.cn; wangzhiyu023@hust.edu.cn.

[2]Department of Mechanical Engineering, School of Engineering, The University of Tokyo, 7-3-1 Hongo, Bunkyo-ku, Tokyo, Japan. E-mail: jean@mech.t.u-tokyo.ac.jp.

Xiaotong Yu and Yuxin Gao contributed equally

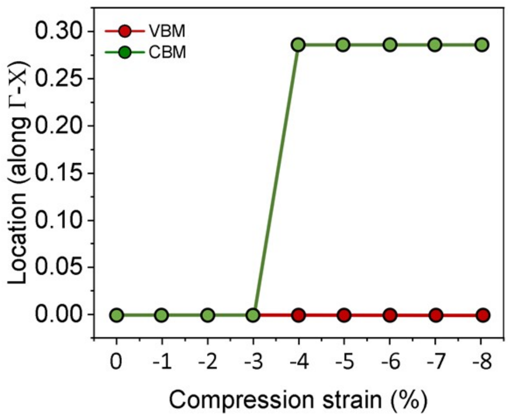

Figure S1. The CBM shifting along the Γ–X direction as a function of the out-of-plane compression strain.

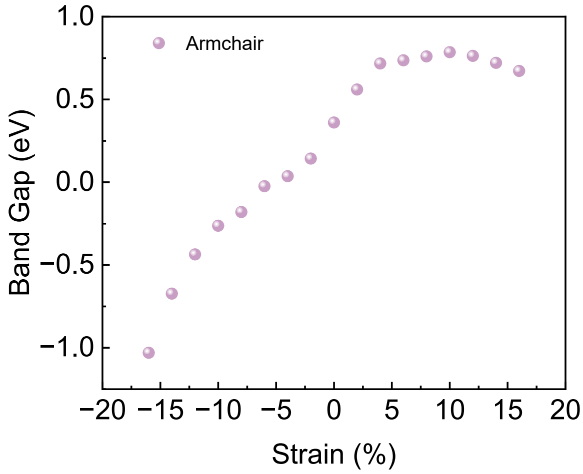

Figure S2. Bandgap engineering in bulk black phosphorus via uniaxial strain along the armchair direction.

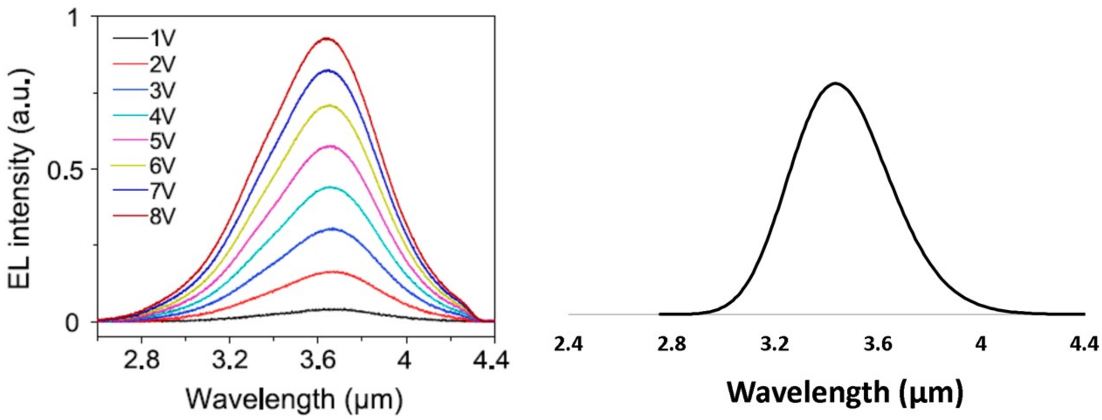

Figure S3. Comparison between (left) the experimentally reported electroluminescence (EL) spectrum and (right) the simulated spectrum from this work [S1].

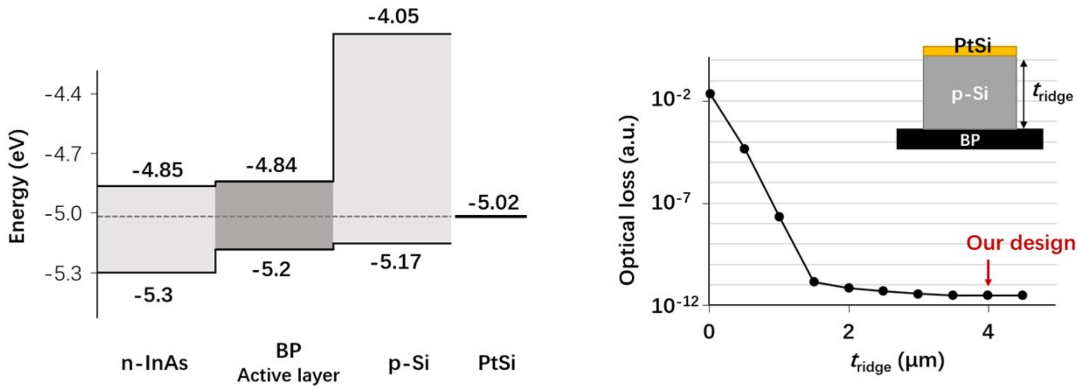

Figure S4. Design details of the BP on-chip emission device: (left) band diagram at thermal equilibrium; (right) optical loss as a function of the p-Si top cladding thickness (t_{ridge}). Electrons flow unimpeded from n-InAs (CBM: -4.85 eV) into the black phosphorus active layer (CBM: -4.84 eV), while holes encounter only a minimal, thermally surmountable 0.03 eV offset from p-Si (VBM: -5.17 eV) into the BP layer (VBM: -5.2 eV). Optical loss is inherently minimized, as the bandgaps of both p-Si and n-InAs are larger than the emission energy, rendering them transparent to the sub-bandgap infrared light emitted from the narrow-gap BP active layer. Combined with the ohmic PtSi/p-Si contact, this design ensures balanced carrier confinement and lossless light extraction through the anode side. Additionally, the distance between the PtSi electrode and the BP active layer is carefully optimized to mitigate absorption loss by the metal. Optical loss calculations as a function of t_{ridge} reveal a clear inflection point at t_{ridge} of 1.5 μm. Similar absorption behavior has been observed in other DFB devices, where t_{ridge} is typically designed to be 2~3 μm [S2-S4]. In our design, a more conservative ridge thickness of 4 μm is adopted to ensure even greater optical isolation.

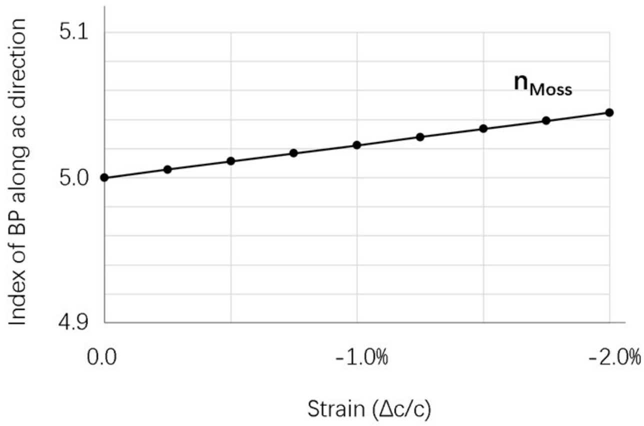

Figure S5. The strain-dependent refractive index of BP along the ac direction as calculated using the Moss formula.

The Moss formula is applied in its small-signal (perturbation) form:

$$n_{Moss} = n - \frac{n}{4E_g}\Delta E_g.$$

It captures the inverse dependence between refractive index and band gap: a reduction in band gap induces an increase in refractive index.

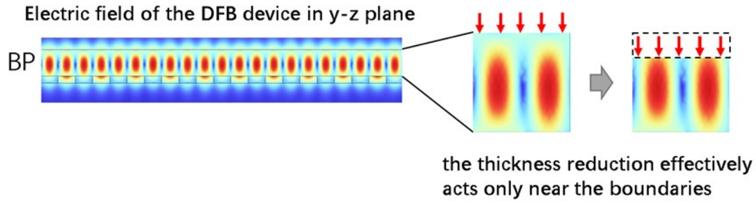

Figure S6. Schematic illustration showing that the thickness reduction under compressive strain effectively reduction in BP effectively acts only the boundaries (where the electric field is weak).

Note S1. Computational Methods

1. DFT calculations

First-principles calculations are performed using DFT as implemented in the Vienna Ab initio Simulation Package (VASP) [S5,S6]. The projector augmented-wave (PAW) method is employed to describe the ion-electron interactions [S7-S9]. To accurately capture the crucial interlayer van der Waals (vdW) interactions in bulk BP under out-of-plane compression, structural relaxations are carried out using the nonlocal vdW density functional optB88-vdW, which has been proven highly reliable for predicting the structural properties of layered phosphorus materials [S10,S11]. An energy cutoff of 500 eV is adopted for the plane-wave expansion of the electronic wave function. The convergence criteria for electronic iterations and ionic relaxations are set to 10^{-5} eV and 0.01 eV/Å, respectively, ensuring high-precision ground-state structures. The Brillouin zone is sampled using a Monkhorst-Pack k-point mesh of $12 \times 8 \times 4$ [S12]. Because standard generalized gradient approximation (GGA) typically underestimates the bandgap of semiconductors, the hybrid functional HSE06 is subsequently employed on the relaxed structures to obtain highly accurate electronic band structures and fundamental gap values under varying out-of-plane strains [S13,S14]

2. Finite element method (FEM) simulations of compressive stress in the BP layer

The macroscopic out-of-plane strain distribution across the BP layer is simulated using the FEM within COMSOL Multiphysics (Solid Mechanics module). To accurately represent the intrinsic mechanical anisotropy of BP, the material is modeled as an orthotropic linear elastic medium. The coordinate system is defined such that the *x*, *y*, and *z* axes align with the armchair, out-of-plane, and zigzag directions, respectively. The Young's modulus is derived from the full stiffness matrix (C_{ij}) calculated via the Tkatchenko-Scheffler (PBE-TS) dispersion correction method [S15]. The utilized values are E_x=31.44 GPa, E_y=30.58 GPa, and E_z=158.94 GPa. Other elastic parameters, including Poisson's ratios and shear moduli, are consistently calculated from the same elastic matrix to ensure physical self-consistency. The bottom boundary of the substrate is set as a fixed constraint, while varying prescribed displacements are applied to the top surface to simulate the mechanical actuation. This approach allows for precise control of the out-of-plane compressive strain (Δc/c).

3. FEM Simulations of DFB optical characteristics

The optical behavior of the DFB device above the transparency threshold is simulated using COMSOL Multiphysics (Wave Optics module). The BP layer is modeled as an anisotropic material with permittivity components ε_x = 25, ε_y = 9, and ε_z = 12, as reported in [S16], where the *x*, *y*, and *z* axes correspond to the armchair, out-of-plane, and zigzag directions, respectively. The refractive indices of other materials are set as n_{InAs} = 3.5, n_{Si} = 3.3, and n_{SiO_2} = 1.4. A two-dimensional domain representing the *y–z* cross-section of the device is used in the simulation, with 1200 periods to achieve a total length of approximately 1 mm. The domain is surrounded by scattering boundary conditions and perfectly matched layers (PMLs) to absorb outgoing waves. The entire domain is meshed using free triangular elements, with a maximum element size of 30 nm for the InAs/SiO_2 grating region. For the remaining areas, the mesh is configured using COMSOL's built-in "extra fine" setting calibrated for general physics. The resonance quality factor is evaluated using an eigenfrequency study. The strain-induced redshift of the emission wavelength is confirmed through both eigenfrequency and wavelength-domain analyses.

Note S2: Lasing Threshold Evaluation of the DFB Device

To assess the practical feasibility of achieving lasing in the proposed structure [S17], we estimate the required carrier injection rate based on the optical properties of bulk BP. The complex permittivity of BP at the peak emission wavelength is taken as [S16]:

$$\varepsilon = \varepsilon_1 + i\varepsilon_2 = 25 + 0.01i$$

From this, the real part of the refractive index is calculated as $n \approx \sqrt{\varepsilon_1} = 5$, and the extinction coefficient is given by $\kappa = \varepsilon_2/2n \approx 1 \times 10^{-3}$. The corresponding material absorption coefficient is then:

$$\alpha_{mat} = \frac{4\pi\kappa}{\lambda} \approx 35.9\ cm^{-1}$$

Other optical losses, such as mirror leakage, are evaluated from the cold-cavity quality factor (Q_{cold} = 2.45 x 10^5, from the COMSOL simulation without material loss)

$$\alpha_{mirror} = \frac{2\pi n}{\lambda Q_{cold}} \approx 0.4\ cm^{-1}$$

Hence, the total cavity loss, $\alpha_{total} = \alpha_{mat} + \alpha_{mirror}$, is estimated to be 36.3 cm^{-1}. At the lasing threshold, the material gain must balance this total loss, i.e., $g_{th} = \alpha_{total} = 36.3\ cm^{-1}$.

In general, the optical gain can be expressed as: $g = a(N - N_{tr})$, where a is the differential gain coefficient (in cm^2) and N_{tr} is the transparency carrier concentration (in cm^{-3}). In the absence of injection (N = 0), the material exhibits absorption, such that $g(0) = -\alpha_{mat} = a(0 - N_{tr})$, yielding $N_{tr} = \alpha_{mat}/a$. At threshold, the gain condition $g_{th} = a(N_{th} - N_{tr})$ gives the threshold carrier concentration:

$$N_{th} = \frac{\alpha_{mat} + g_{th}}{a} \#(1)$$

Following standard semiconductor laser theory, the differential gain coefficient can be related to the radiative recombination lifetime τ_{rad} and the spontaneous emission linewidth $\Delta\nu$ (ignoring the optical confinement factor for simplicity and assuming λ_{EL} aligns with λ_{DFB} at λ) [S18]:

$$a = \frac{\lambda^2}{8\pi n^2 \tau_{rad} \Delta\nu}$$

Since the radiative lifetime is related to the radiative recombination coefficient B by $\tau_{rad} = 1/BN$, at threshold we have:

$$a = \frac{\lambda^2 B N_{th}}{8\pi n^2 \Delta\nu} \#(2)$$

Substituting (2) into (1) yields an expression for the product BN_{th}^2:

$$BN_{th}^2 = (\alpha_{mat} + g_{th}) \frac{8\pi n^2 \Delta\nu}{\lambda^2} \#(3)$$

The carrier injection rate G required to sustain the threshold carrier density is then given by $G = \frac{BN_{th}^2}{QY}$, where QY is the internal quantum yield. Combining this with (3), we obtain:

$$G = \frac{BN_{th}^2}{QY} = \frac{(\alpha_{mat} + g_{th})\frac{8\pi n^2 \Delta\nu}{\lambda^2}}{QY} \#(4)$$

To evaluate G numerically, we adopt parameter values informed by the theoretical analysis in [S18]. The Auger recombination coefficient is exceptionally low (on the order of 10^{-44} cm^6 s^{-1}), leading to a weak dependence of QY on G. For a bare BP layer with a thickness of 590 nm, the QY_0 is estimated to be ~1% for *G* between 10^{-24} and $10^{-27}$$cm^{-3}$ s^{-1}. The Purcell factor of the BP in the DFB device is calculated as

$$F_P = \frac{3}{4\pi^2}\frac{Q}{V_{mode}}\left(\frac{\lambda}{n}\right)^3 \approx 0.9$$

The QY of the BP in the DFB device is then given by:

$$QY = \frac{F_P}{F_P + \frac{1}{QY_0} - 1} \approx 0.9\%$$

The spontaneous emission linewidth of BP is taken as $\Delta\lambda$ = 500 nm. Substituting these values into Eq. (4) yields: $G \approx 1.58 \times 10^{26}\ cm^{-3}s^{-1}$. We compare this estimated G value (corresponding to $P_{th,0}$ of 8.4 mW) with experimental data from a BP laser reported in [S17], where the time-averaged G is reported to exceed 1.5×10^{25} cm^{-3} s^{-1} for a pulsed laser-pumped device. The corresponding transient G is estimated to be at least on the order of 10^{27} or 10^{28} cm^{-3} s^{-1}. Our estimated value falls well within the range of injection rates that are experimentally achievable in practical semiconductor laser structures under realistic operating conditions.

References:

S1. Chang, Tian-Yun, et al. “Black phosphorus mid-infrared light-emitting diodes integrated with silicon photonic waveguides.” *Nano Letters* 20.9 (2020): 6824-6830.

S2. Briggs, Ryan M., et al. "Single-mode 2.65 µm InGaAsSb/AlInGaAsSb laterally coupled distributed-feedback diode lasers for atmospheric gas detection." *Optics Express* 21.1 (2013): 1317-1323.

S3. Forouhar, Siamak, et al. "High-power laterally coupled distributed-feedback GaSb-based diode lasers at 2 µm wavelength." *Applied Physics Letters* 100.3 (2012).

S4. Chen, Woo-Young, Choi C., and Clifton G. Fonstad. "Evaluation of coupling coefficients for laterally-coupled distributed feedback lasers." *Japanese Journal of Applied Physics* 35.9R (1996): 4654.

S5. Kresse, Georg, and Jürgen Furthmüller. "Efficient iterative schemes for ab initio total-energy calculations using a plane-wave basis set." *Physical Review B* 54.16 (1996): 11169.

S6. Kresse, Georg, and Jürgen Furthmüller. "Efficiency of ab-initio total energy calculations for metals and semiconductors using a plane-wave basis set." *Computational Materials Science* 6.1 (1996): 15-50.

S7. Blöchl, Peter E. "Projector augmented-wave method." *Physical Review B* 50.24 (1994): 17953.

S8. Kresse, Georg, and Jürgen Hafner. "Ab initio molecular dynamics for liquid metals." *Physical Review B* 47.1 (1993): 558.

S9. Perdew, John P., Kieron Burke, and Matthias Ernzerhof. "Generalized gradient approximation made simple." *Physical Review Letters* 77.18 (1996): 3865.

S10. Klimeš, Jiří, David R. Bowler, and Angelos Michaelides. "Chemical accuracy for the van der Waals density functional." *Journal of Physics: Condensed Matter* 22.2 (2010): 022201.

S11. Klimeš, Jiří, David R. Bowler, and Angelos Michaelides. "Van der Waals density functionals applied to solids." *Physical Review B—Condensed Matter and Materials Physics* 83.19 (2011): 195131.

S12. Monkhorst, Hendrik J., and James D. Pack. "Special points for Brillouin-zone integrations." *Physical Review B* 13.12 (1976): 5188.

S13. Li, Yan, Shengxue Yang, and Jingbo Li. "Modulation of the electronic properties of ultrathin black phosphorus by strain and electrical field." *The Journal of Physical Chemistry C* 118.41 (2014): 23970-23976.

S14. Heyd, Jochen, Gustavo E. Scuseria, and Matthias Ernzerhof. "Hybrid functionals based on a screened Coulomb potential." *The Journal of Chemical Physics* 118.18 (2003): 8207-8215.

S15. Appalakondaiah, S., et al. "Effect of van der Waals interactions on the structural and elastic properties of black phosphorus." *Physical Review B—Condensed Matter and Materials Physics* 86.3 (2012): 035105.

S16. Schué, Léonard, et al. "Visible out-of-plane polarized luminescence and electronic resonance in black phosphorus." *Nano Letters* 22.7 (2022): 2851-2858.

S17. Zhang, Yushuang, et al. "Wavelength-tunable mid-infrared lasing from black phosphorus nanosheets." *Advanced Materials* 32.17 (2020): 1808319.

S18. Coldren, L. A., Corzine, S. W., & Mašanović, M. L. (2012). *Diode Lasers and Photonic Integrated Circuits*. Wiley.